

Secular Evolution of PSR J2021+4026: Long-Term γ -Ray Flux and Spin-Down Variability Beyond State Transitions

XUE-ZHI LIU,^{1,2,3} MING-YU GE,^{3,4} XIAO-PING ZHENG,^{1,2} XIAO-BO LI,^{3,4} HAN-LONG PENG,⁵ WEN-TAO YE,^{3,4} BO-YAN CHEN,^{3,4} SHI-JIE ZHENG,^{3,4} FANG-JUN LU,³ AND SHUANG-NAN ZHANG^{3,4}

¹*Laboratory for Compact Object Astrophysics and AstroSpace Technology, Central China Normal University, Wuhan 430079, People's Republic of China;
 xz_liu@mails.ccnu.edu.cn; zhxp@ccnu.edu.cn*

²*Institute of Astrophysics, Central China Normal University, Wuhan 430079, People's Republic of China*

³*State Key Laboratory of Particle Astrophysics, Institute of High Energy Physics, Chinese Academy of Sciences, Beijing 100049, People's Republic of China;
 gemy@ihep.ac.cn*

⁴*University of Chinese Academy of Sciences, Chinese Academy of Sciences, Beijing 100049, People's Republic of China*

⁵*School of Physics and Technology, Nanjing Normal University, Nanjing, 210023, Jiangsu, People's Republic of China*

(Received 2025 December 29; Revised ...; Accepted ...; Published ...)

ABSTRACT

PSR J2021+4026 is a remarkable γ -ray pulsar exhibiting repeated transitions between high γ -ray flux (HGF) and low γ -ray flux (LGF) states. With 17-yr *Fermi*-LAT monitoring, we reveal persistent secular evolution and enhanced spin-down rate variability *within* individual emission states—beneath the quasi-periodic state transitions. After removing discrete jumps, the jump-corrected flux δF_γ shows a three-phase evolution: rise ($+2.02^{+0.17\%}_{-0.15\%}$ yr $^{-1}$), decline ($-3.72^{+0.34\%}_{-0.47\%}$ yr $^{-1}$), and rapid rise ($+14.9^{+6.4\%}_{-4.4\%}$ yr $^{-1}$), with all rates quoted relative to the long-term mean flux $\langle F_\gamma \rangle = 7.8 \times 10^{-10}$ erg cm $^{-2}$ s $^{-1}$. Moreover, the flux of the LGF state is gradually approaching the stable HGF level at a rate of $+0.72 \pm 0.11\%$ yr $^{-1}$. These results demonstrate that secular flux evolution in PSR J2021+4026 operates largely independently of discrete state transitions, yet jointly with them drives the system toward a stable high-flux equilibrium.

Keywords: gamma rays: stars — pulsars: individual (PSR J2021+4026) — stars: neutron

1. INTRODUCTION

PSR J2021+4026 is one of the brightest γ -ray pulsars discovered by the *Fermi* Large Area Telescope (LAT) in blind searches (Atwood et al. 2009; Abdo et al. 2009). It has a spin frequency $\nu \sim 3.8$ Hz, spin-down rate $|\dot{\nu}| \sim 8 \times 10^{-13}$ Hz s $^{-1}$, and characteristic age $\tau_c = 77$ kyr, with a double-peaked γ -ray pulse profile. An extended X-ray pulse peak is seen in *XMM-Newton* observations (Lin et al. 2013), and the pulsar may be associated with the \sim 6.6-kyr-old supernova remnant G78.2+2.1 (Trepel et al. 2010). Notably, PSR J2021+4026 is radio-quiet (Shaw et al. 2023) yet exhibits state transitions—manifested as quasi-periodic, correlated variations in γ -ray flux F_γ , $\dot{\nu}$, and pulse shape—phenomena commonly observed in radio pulsars and thought to be linked to magnetospheric reconfigurations (Kramer et al. 2006; Hobbs et al. 2010; Lyne et al. 2010), but exceptionally rare among γ -ray pulsars (Allafort et al. 2013).

For most of the time, PSR J2021+4026 resides in either a stable high γ -ray flux (HGF) state with low $|\dot{\nu}|$ and an emerging bridge component between the two pulse peaks, or a low γ -ray flux (LGF) state with elevated $|\dot{\nu}|$. However, during five observed state transitions—occurring approximately every 3 years—the pulsar transitions rapidly between states:

HGF \leftrightarrow LGF switches take place within \sim 30-day, accompanied by \sim 20% variations in F_γ and \sim 4% changes in $|\dot{\nu}|$ (Allafort et al. 2013; Ng et al. 2016; Takata et al. 2020; Fiori et al. 2024; Wang et al. 2023).

The apparent discontinuities in $\dot{\nu}$ during state transitions have led to glitch-inspired explanations, such as an increase in magnetic inclination angle caused by plates movement (Ng et al. 2016). Meanwhile, the quasi-periodic behavior of flux and spin-down rate has motivated interpretations invoking damped free precession of the neutron star (Takata et al. 2020; Tong & Wang 2025). Multiwavelength observations further reveal a concurrent phase shift in the X-ray pulsations, hinting at a non-dipolar (e.g., quadrupolar) contribution to the magnetic field geometry (Razzano et al. 2023; Fiori et al. 2024). Yet a comprehensive picture of the long-term variability of PSR J2021+4026 remains elusive.

It should be noted that, in the first HGF state, Allafort et al. (2013) reported a \sim 3-yr gradual flux increase prior to the transition and suggested a possible link to free precession (Jones 2012); however, no similar long-term intra-state evolution has since been reported. While Zhao et al. (2017) and Fiori et al. (2024) modeled the \sim 150-day post-transition flux recovery with a linear trend, they did not assume secular variation throughout the entire emission state. Lever-

aging the full 17-yr *Fermi*-LAT dataset and removing discrete state jumps, we reveal persistent secular variation in F_γ —correlated with $\dot{\nu}$ variability—*within* individual emission states, beneath the quasi-periodic state transitions.

2. DATA REDUCTION

Our data are collected from August 5, 2008, to November 5, 2025, including LAT photons in the class of P8R3_SOURCE_V3, selected within a 15° -radius centered on the J2000 *Chandra* position of PSR J2021+4026 (Weisskopf et al. 2011). Data are in the energy range from 100 MeV to 300 GeV, with zenith angles $z < 90^\circ$.

For the flux analysis, we filtered the good time intervals by the command `DATA_QUAL>0 && LAT_CONFIG==1`, restricted events to the Galactic point-source class (`evclass = 128`) and included both front- and back-converting events (`evtype = 3`). A binned likelihood analysis was performed, with the data divided into 35 logarithmically spaced energy bins (10 bins per decade) and spatial pixels of $0.1^\circ \times 0.1^\circ$.

For the timing analysis, we further confined the photon sample to a 1° -radius circular region around the source position and applied barycentric correction using the JPL DE405 solar system ephemeris.

3. FLUX AND TIMING ANALYSIS

Binned likelihood analyses were conducted for each state and for consecutive 30-day intervals, via *fermipy* v1.4.0 (Wood et al. 2018) and *Fermi* tools v2.4.0, using the 4FGL-DR4 catalog (Abdollahi et al. 2022; Ballet et al. 2023) as the source model, where PSR J2021+4026 was described by a power law with exponential cutoff:

$$\frac{dN}{dE} = \begin{cases} N_0 \left(\frac{E}{E_0} \right)^{\gamma_0 - \frac{d}{2} \ln \frac{E}{E_0} - \frac{db}{6} \ln^2 \frac{E}{E_0} - \frac{db^2}{24} \ln^3 \frac{E}{E_0}}, \\ \text{if } |b \ln \frac{E}{E_0}| < 10^{-2}; \\ N_0 \left(\frac{E}{E_0} \right)^{\gamma_0 + d/b} \exp \left(\frac{d}{b^2} \left(1 - \left(\frac{E}{E_0} \right)^b \right) \right), \\ \text{otherwise.} \end{cases} \quad (1)$$

The spectral parameters include the spectral slope $\gamma_0 = d \log(dN/dE)/d \log E$ and the second derivative $-d = d^2 \log(dN/dE)/d(\log E)^2$ at $E_0 = 1.8$ GeV. The exponent index b is fixed to 0.39.

We included all sources within a $25^\circ \times 25^\circ$ region centered on PSR J2021+4026, together with the Galactic and isotropic diffuse emission templates. The spectral parameters of PSR J2021+4026 and the two diffuse components, and the normalizations of variable sources (`Variability_Index > 18` within 7°) and an extended source (G78.2+2.1) were freed in all fits. For each state, we identified sources with `TS > 20` within 5° and freed their

normalizations. Specifically, the total numbers of free parameters from the first to the last state are: 30, 31, 31, 32, 28, 30, 27, and 30. This same set of freed parameters was then applied consistently to all 30-day intervals within the respective state.

Segmented timing analyses were performed with a second-order Taylor expansion model:

$$\Phi - \Phi_0 = \nu(t - t_0) + \frac{1}{2} \dot{\nu}(t - t_0)^2, \quad (2)$$

where Φ_0 , ν , and $\dot{\nu}$ denote the phase, spin frequency, and frequency derivative at the reference epoch t_0 , respectively. The length of each interval was determined adaptively based on the significance of the folded pulse profile, spanning from 40-day to 150-day.

Following timing ephemerides from Wang et al. (2023), we folded pulse profiles and derived times-of-arrival (TOAs) from best frequencies. Once four or five TOAs were obtained, we fitted them with TEMPO2 (Hobbs et al. 2006) to generate short-term ephemerides. Further details of the timing procedure can be found in Ge et al. (2019).

4. RESULTS

Relative to the mean flux $\langle F_\gamma \rangle$, the concurrent jumps in F_γ and $\dot{\nu}$ (Figure 1), together with the associated pulse profile changes (Figure 2), confirm seven state transitions over the 17-yr baseline—two more than reported by Wang et al. (2023). Following the convention of Fiori et al. (2024), we label the states sequentially with capital letters A through H and mark the transition epochs with dotted lines in both figures; detailed spectral and timing properties are provided in Table 1 and the Zenodo repository (Liu et al. 2025)¹.

To quantify intra-state evolution, we performed minimum χ^2 linear fits to the 30-day binned flux in each state. The resulting flux evolution rates (R_{state}), expressed relative to $\langle F_\gamma \rangle$ of each state, and inter-state flux jumps ($\Delta F_\gamma = F_{\gamma,\text{end}}^{(\text{prev})} - F_{\gamma,\text{start}}^{(\text{next})}$), derived from the best-fit parameters, are summarized in Table 1. In addition to the gradual rise in state A, several other states exhibit non-zero R_{state} values, (e.g., $R_{\text{state}} = +15\% \pm 4\% \text{ yr}^{-1}$ in state H), indicating that the long-term flux evolution observed in state A is not isolated, but likely a persistent characteristic of PSR J2021+4026.

We further aligned adjacent states vertically by removing the flux jumps ΔF_γ and the mean offset, producing the jump-corrected light curve δF_γ shown in Figure 1(b). A fit of the entire light curve δF_γ with a constant flux model yields $\chi^2_{\text{red}} = 2.21$ for 208 degrees of freedom, significantly exceeding the expected value of unity and confirming that

¹ <https://doi.org/10.5281/zenodo.18060028>

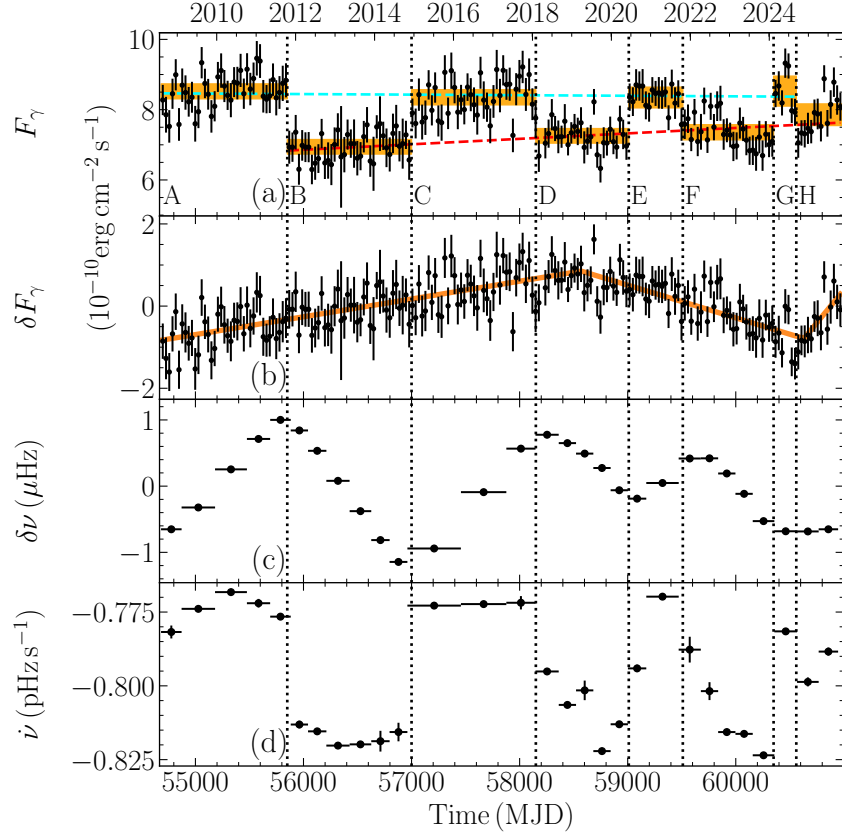


Figure 1. Energy flux and spin evolution of PSR J2021+4026. Panel (a): 30-day binned flux measurements with 1σ uncertainties (black points) and per-state fluxes with 3σ confidence intervals (orange bands). The cyan and red dashed lines are the linear fits to the fluxes in the HGF and LGF states respectively. Panel (b): Jump-corrected flux δF_γ , obtained by removing the mean offset and inter-state flux jumps; the orange piecewise linear curve shows the best fit to the secular evolution. Panels (c) and (d): Timing evolution in ν and $\dot{\nu}$; panel (c) displays the timing residuals $\delta\nu$ after subtracting the linear trend and mean offset. Vertical and horizontal error bars indicate 1σ uncertainties and ephemeris time spans, respectively. Vertical dotted lines mark the state transitions reported in [Fiori et al. \(2024\)](#); [Wang et al. \(2023\)](#) and this work.

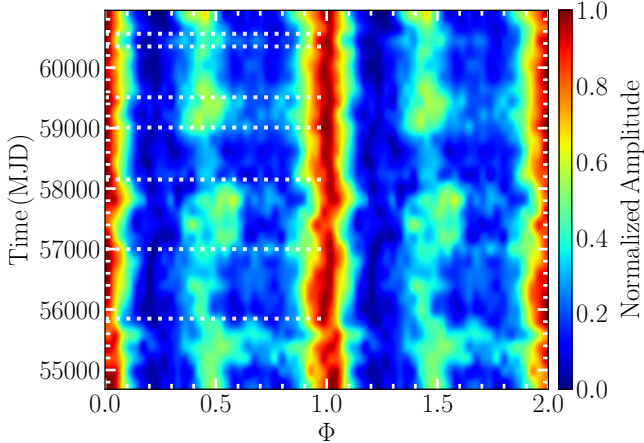


Figure 2. Two-dimensional histogram of the normalized pulse profile versus time, with phases and time each divided into 32 bins and 31 bins, smoothed via Gaussian interpolation. Horizontal dotted lines mark the state transitions. The main pulse, aligned to phase 0, is indicated in red.

δF_γ deviates from a constant level. In contrast, a continuous piecewise linear model defined by 6 parameters provides an excellent description with $\chi^2_{\text{red}} = 0.91$ (203 d.o.f.). The best-fit solution comprises three distinct phases—a ~ 10 -yr rise, a ~ 6 -yr decline, and a recent ~ 1 -yr rapid rise—with phase-averaged rates of $R_{\text{phase}} = +2.02^{+0.17\%} \text{ yr}^{-1}$, $-3.72^{+0.34\%} \text{ yr}^{-1}$, and $+14.9^{+6.4\%} \text{ yr}^{-1}$, and transition epochs at MJD 58570^{+110}_{-93} and MJD 60631^{+62}_{-65} . Because the slope parameters and transition epochs are strongly correlated in the piecewise linear fit, we estimated their uncertainties using a residual bootstrap method; the asymmetric errors quoted correspond to the 16th and 84th percentiles of the bootstrap distributions.

Accompanying the intra-state flux evolution, $\dot{\nu}$ exhibits enhanced variability in states D–F, in contrast to the relatively stable spin-down rates in states A–C (Figure 1(d)). Notably, the total $\dot{\nu}$ variation in state F is comparable in magnitude to the discrete jumps at the A–C transitions. Moreover, the elevated timing noise (MJD 58150–60350) coincides with

the flux-decline phase, further supporting a physical link between secular flux evolution and spin-down behavior.

Additionally, despite intra-state flux variations and non-monotonic jump amplitudes, the long-term flux levels of the HGF states remain stable, whereas those of the LGF states show a gradual increase toward the HGF level—as illustrated by the orange confidence bands in Figure 1(a). Linear fits to all 30-day binned fluxes of HGF and LGF (cyan and red dashed lines) yield evolution rates of $R_{\text{HGF}} = -0.08 \pm 0.11\% \text{ yr}^{-1}$ and $R_{\text{LGF}} = +0.72 \pm 0.11\% \text{ yr}^{-1}$, respectively. This differential evolution—arising from the interplay of discrete state transitions and secular trends—suggests that PSR J2021+4026 is undergoing a dissipative relaxation toward a stable HGF equilibrium state. Extrapolation indicates that the HGF and LGF flux levels will converge near MJD 65250 (2037).

5. DISCUSSION AND SUMMARY

Beyond the discrete flux jumps at state transitions, the intra-state variability and three-phase secular evolution uncovered here add a new dimension to the long-term behavior of PSR J2021+4026. This suggests that the magnetic inclination angle or polar-cap magnetospheric configuration (Ng et al. 2016; Zhao et al. 2017; Fiori et al. 2024) may undergo changes—both abrupt and gradual. We caution, however, that our analysis treats state transitions as instantaneous and discontinuous events; future work will be needed to assess whether they possess short-term aftereffects that could influence the inferred secular evolution.

In its flux evolution, PSR J2021+4026 displays two secular features: a quasi-oscillatory variation of δF_γ and a systematic convergence of LGF toward the stable HGF level. These characteristics share qualitative similarities with the oscillatory and dissipative aspects of damping precession (Tong & Wang 2025). Yet, the increase in $|R_{\text{phase}}|$ over time and the stability of the HGF state are not naturally explained within that framework, suggesting that additional complexities in the magnetospheric or interior dynamics of PSR J2021+4026 may be at play. Using the upper limit on $\Delta\nu$ and the measured $\Delta\nu$ at the state transitions, Zhao et al. (2017) found that the relative changes $\Delta\nu/\nu$ and $\Delta\nu/\dot{\nu}$ in PSR J2021+4026 are consistent with the range observed in glitches for young pulsars. Nevertheless, we find that when $R_{\text{phase}} < 0$, the variability of $\dot{\nu}$ within each state is enhanced, which further increases the difficulty of distinguishing potential glitch signatures at the D–F state transitions.

It is worth noting that Razzano et al. (2023) reported a ~ 0.25 phase lag in the X-ray pulse profile of PSR J2021+4026 between two *XMM-Newton* observations separated by 3.7 yr, spanning the B–C state transition epoch. They interpreted this shift as a reconfiguration of the cou-

pling between the near-surface quadrupole magnetic field and the large-scale dipole component. However, apart from this isolated shift, no significant spectral or morphological variability has been detected in the X-ray emission (Wang et al. 2018), which possesses the largest known γ -ray-to-X-ray flux ratio ($\sim 6.5 \times 10^4$) (Hui et al. 2017). This decoupling may reflect a special magnetospheric (Fiori et al. 2024), or it could be just limited by the precision of observations.

Both the Crab and Vela pulsars exhibit glitches but no state transitions; an observable long-term decline in X-ray flux is seen in Crab, correlated with its decreasing spin-down luminosity (Yan et al. 2018; Wang et al. 2023). In contrast, for PSR J2021+4026, the relationship between flux and spin evolution is more complex, as detailed in Appendix. State transitions are more common in radio pulsars and are classified as one type of timing noise, attributed to magnetospheric reconfigurations (Kramer et al. 2006; Lyne et al. 2010). A comparable case is PSR J1124–5916—a young pulsar with radio and γ -ray pulsations that exhibits $\dot{\nu}$ -state transitions and, owing to its low timing noise, has yielded a precise braking index measurement (Ge et al. 2020). However, unlike PSR J2021+4026, its state transitions show no detectable changes in F_γ or pulse profile, and its spin evolution is likely dominated by magnetic dipole radiation and pulsar wind. Similarly, PSR B0943+10 shows correlated radio and X-ray state switching—accompanied by profile transformations—yet displays no significant change in spin properties (Hermsen et al. 2013).

To advance our understanding of state transitions, secular evolution, and their relationship with spin-down behavior, coordinated multiwavelength monitoring—especially in X-rays—is essential. The *Einstein Probe* (EP; Yuan et al. 2022, 2025), and the upcoming missions *enhanced X-ray Timing and Polarimetry mission* (eXTP; Zhang et al. 2025; Ge et al. 2025) will enable high-precision pulse profile and polarization measurements over the next decade. Sustained, simultaneous coverage by *Fermi*-LAT and these X-ray facilities is key to unraveling the physical linkage between γ -ray and X-ray emission processes in pulsars.

ACKNOWLEDGMENTS

This work is supported by the China’s Space Origins Exploration Program and the National Natural Science Foundation of China (Grant Nos. 12373051, 12033001, 12273043, 12473039). We acknowledge the use of the public data from the *Fermi*-LAT data archive. We thank Yu-Long Yan, Qian Zhang, Pei-Xin Zhu and Jia-Chen Xie for helpful discussions on pulsar precession and glitch phenomena.

Table 1. Spectral parameters and the flux variations of PSR J2021+4026 in different states.

Parameter	A	B	C	D	E	F	G	H
Start	54683	55850	57000	58150	59010	59510	60350	60560
Stop	55850	57000	58150	59010	59510	60350	60560	60984
F_γ^a	8.52(7)	6.94(7)	8.35(7)	7.26(7)	8.3(1)	7.36(7)	8.5(1)	7.9(1)
$F_{\gamma,\text{pho}}^b$	1.09(1)	0.95(1)	1.08(1)	1.00(1)	1.11(2)	1.01(1)	1.15(3)	1.04(2)
γ_0	-2.49(1)	-2.61(2)	-2.52(1)	-2.61(2)	-2.49(2)	-2.59(2)	-2.52(3)	-2.54(2)
d	0.75(2)	0.81(2)	0.77(2)	0.80(2)	0.69(2)	0.77(2)	0.72(3)	0.77(3)
R_{state}^c	2.6 ± 1.0	1.7 ± 1.0	2.3 ± 1.0	-0.9 ± 1.5	-3.1 ± 3.2	-4.4 ± 1.5	-11 ± 11	15 ± 4
ΔF_γ^d		-2.1	0.88	-1.3	1.4	-0.43	1.8	-1.2

NOTE—The numbers in the parentheses denote the 1σ errors in the last digit.

a Energy flux in units of 10^{-10} erg cm $^{-2}$ s $^{-1}$.

b Photon flux in units of 10^{-6} photon cm $^{-2}$ s $^{-1}$.

c Relative changing rate of flux in units of percentage per year.

d Jump of energy flux from the previous state in units of 10^{-10} erg cm $^{-2}$ s $^{-1}$.

APPENDIX

To investigate a potential connection between δF_γ and spin behavior, we constructed a time series of $\delta|\dot{\nu}|$ following an analogous procedure to that used for δF_γ , aiming to remove the influence of discrete state transitions. However, due to the limited number of timing epochs, the difference in $|\dot{\nu}|$ between the two states was simply taken as the difference between two adjacent measurements. To enable a direct comparison, we also resampled the original δF_γ light curve using weighted averages over time intervals matched to those of the $\dot{\nu}$, resulting in 29 data points for both δF_γ and $\delta|\dot{\nu}|$.

As shown in Figure 3, a visual inspection reveals little correspondence between δF_γ and $\delta|\dot{\nu}|$. Quantitatively, their Pearson correlation coefficient is -0.093 with a p -value of 0.631 , indicating no significant linear correlation. In contrast, when the same resampling is applied to the F_γ , we find a strong anti-correlation with $|\dot{\nu}|$: the Pearson coefficient is -0.91 (p -value $\sim 10^{-12}$). This stark difference highlights the complexity of the relationship between γ -ray emission and spin-down evolution in PSR J2021+4026.

REFERENCES

Abdo, A. A., Ackermann, M., Ajello, M., et al. 2009, Science, 325, 840, doi: [10.1126/science.1175558](https://doi.org/10.1126/science.1175558)

Abdollahi, S., et al. 2022, Astrophys. J. Supp., 260, 53, doi: [10.3847/1538-4365/ac6751](https://doi.org/10.3847/1538-4365/ac6751)

Allafort, A., et al. 2013, Astrophys. J. Lett., 777, L2, doi: [10.1088/2041-8205/777/1/L2](https://doi.org/10.1088/2041-8205/777/1/L2)

Atwood, W. B., et al. 2009, Astrophys. J., 697, 1071, doi: [10.1088/0004-637X/697/2/1071](https://doi.org/10.1088/0004-637X/697/2/1071)

Ballet, J., Bruel, P., Burnett, T. H., & Lott, B. 2023, <https://arxiv.org/abs/2307.12546>

Fiori, A., Razzano, M., Harding, A. K., et al. 2024, Astron. Astrophys., 685, A70, doi: [10.1051/0004-6361/202348924](https://doi.org/10.1051/0004-6361/202348924)

Ge, M., et al. 2025, Sci. China Phys. Mech. Astron., 68, 119505, doi: [10.1007/s11433-025-2796-y](https://doi.org/10.1007/s11433-025-2796-y)

Ge, M. Y., Lu, F. J., Yan, L. L., et al. 2019, Nature Astron., 3, 1122, doi: [10.1038/s41550-019-0853-5](https://doi.org/10.1038/s41550-019-0853-5)

Ge, M. Y., Yuan, J. P., Lu, F. J., et al. 2020, Astrophys. J. Lett., 900, L7, doi: [10.3847/2041-8213/abaeed](https://doi.org/10.3847/2041-8213/abaeed)

Hermes, W., Hessels, J. W. T., Kuiper, L., et al. 2013, Science, 339, 436, doi: [10.1126/science.1230960](https://doi.org/10.1126/science.1230960)

Hobbs, G., Edwards, R., & Manchester, R. 2006, Mon. Not. Roy. Astron. Soc., 369, 655, doi: [10.1111/j.1365-2966.2006.10302.x](https://doi.org/10.1111/j.1365-2966.2006.10302.x)

Hobbs, G., Lyne, A. G., & Kramer, M. 2010, Mon. Not. Roy. Astron. Soc., 402, 1027, doi: [10.1111/j.1365-2966.2009.15938.x](https://doi.org/10.1111/j.1365-2966.2009.15938.x)

Hui, C. Y., Lee, J., Takata, J., Ng, C. W., & Cheng, K. S. 2017, Astrophys. J., 834, 120, doi: [10.3847/1538-4357/834/2/120](https://doi.org/10.3847/1538-4357/834/2/120)

Jones, D. I. 2012, Mon. Not. Roy. Astron. Soc., 420, 2325, doi: [10.1111/j.1365-2966.2011.20238.x](https://doi.org/10.1111/j.1365-2966.2011.20238.x)

Kramer, M., Lyne, A. G., O’Brien, J. T., Jordan, C. A., & Lorimer, D. R. 2006, Science, 312, 549, doi: [10.1126/science.1124060](https://doi.org/10.1126/science.1124060)

Lin, L. C. C., et al. 2013, Astrophys. J. Lett., 770, L9, doi: [10.1088/2041-8205/770/1/L9](https://doi.org/10.1088/2041-8205/770/1/L9)

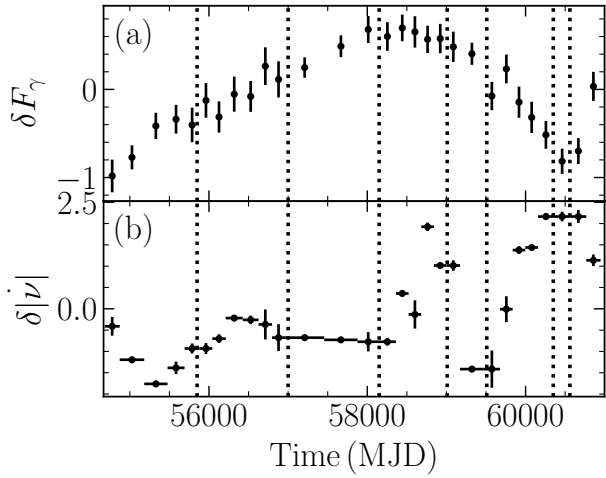


Figure 3. Panel (a): Resampled δF_γ from weighted averages, in units of $10^{-10} \text{ erg cm}^{-2} \text{ s}^{-1}$. Panel (b): Jump-corrected $\delta |\dot{\nu}|$ in units of $10^{-14} \text{ Hz s}^{-1}$, obtained by subtracting the inter-state timing jumps and mean offset. Dotted lines mark the state transitions.

Liu, X., Ge, M., Zheng, X., et al. 2025, The ephemerides and pulse profiles of PSR J2021+4026 from 2008 to 2025, Zenodo, doi: [10.5281/zenodo.18060028](https://doi.org/10.5281/zenodo.18060028)

Lyne, A., Hobbs, G., Kramer, M., Stairs, I., & Stappers, B. 2010, Science, 329, 408, doi: [10.1126/science.1186683](https://doi.org/10.1126/science.1186683)

Ng, C. W., Takata, J., & Cheng, K. S. 2016, Astrophys. J., 825, 18, doi: [10.3847/0004-637X/825/1/18](https://doi.org/10.3847/0004-637X/825/1/18)

Razzano, M., Fiori, A., Saz Parkinson, P. M., et al. 2023, Astron. Astrophys., 676, A91, doi: [10.1051/0004-6361/202345873](https://doi.org/10.1051/0004-6361/202345873)

Shaw, B., Stappers, B. W., Weltevrede, P., et al. 2023, Mon. Not. Roy. Astron. Soc., 523, 568, doi: [10.1093/mnras/stad1419](https://doi.org/10.1093/mnras/stad1419)

Takata, J., Wang, H. H., Lin, L. C. C., et al. 2020, doi: [10.3847/1538-4357/ab67b1](https://doi.org/10.3847/1538-4357/ab67b1)

Tong, H., & Wang, H. H. 2025, Astrophys. J., 980, 232, doi: [10.3847/1538-4357/adaf1d](https://doi.org/10.3847/1538-4357/adaf1d)

Trepl, L., Hui, C. Y., Cheng, K. S., et al. 2010, Mon. Not. Roy. Astron. Soc., 405, 1339, doi: [10.1111/j.1365-2966.2010.16555.x](https://doi.org/10.1111/j.1365-2966.2010.16555.x)

Wang, H. H., Takata, J., Hu, C. P., Lin, L. C. C., & Zhao, J. 2018, Astrophys. J., 856, 98, doi: [10.3847/1538-4357/aab202](https://doi.org/10.3847/1538-4357/aab202)

Wang, H. H., Takata, J., Lin, L. C. C., & Tam, P. H. T. 2023, Mon. Not. Roy. Astron. Soc., 527, 12016, doi: [10.1093/mnras/stad3899](https://doi.org/10.1093/mnras/stad3899)

Weisskopf, M. C., et al. 2011, Astrophys. J., 743, 74, doi: [10.1088/0004-637X/743/1/74](https://doi.org/10.1088/0004-637X/743/1/74)

Wood, M., Caputo, R., Charles, E., et al. 2018, PoS, ICRC2017, 824, doi: [10.22323/1.301.0824](https://doi.org/10.22323/1.301.0824)

Yan, L. L., Ge, M. Y., Lu, F. J., et al. 2018, Astrophys. J., 865, 21, doi: [10.3847/1538-4357/aad911](https://doi.org/10.3847/1538-4357/aad911)

Yuan, W., Zhang, C., Chen, Y., & Ling, Z. 2022, doi: [10.1007/978-981-16-4544-0_151-1](https://doi.org/10.1007/978-981-16-4544-0_151-1)

Yuan, W., et al. 2025, Sci. China Phys. Mech. Astron., 68, 239501, doi: [10.1007/s11433-024-2600-3](https://doi.org/10.1007/s11433-024-2600-3)

Zhang, S.-N., et al. 2025, Sci. China Phys. Mech. Astron., 68, 119502, doi: [10.1007/s11433-025-2786-6](https://doi.org/10.1007/s11433-025-2786-6)

Zhao, J., et al. 2017, Astrophys. J., 842, 53, doi: [10.3847/1538-4357/aa74d8](https://doi.org/10.3847/1538-4357/aa74d8)